

# Hardware-efficient quantum random access memory with hybrid quantum acoustic systems

Connor T. Hann,<sup>1</sup> Chang-Ling Zou,<sup>2</sup> Yaxing Zhang,<sup>1</sup> Yiwen Chu,<sup>3</sup>  
Robert J. Schoelkopf,<sup>1</sup> Steven M. Girvin,<sup>1</sup> and Liang Jiang<sup>1</sup>

<sup>1</sup>*Departments of Applied Physics and Physics, Yale University, New Haven, Connecticut 06511, USA*

<sup>2</sup>*Key Laboratory of Quantum Information, CAS,*

*University of Science and Technology of China, Hefei, China.*

<sup>3</sup>*Department of Physics, ETH Zürich, 8093 Zürich, Switzerland*

Hybrid quantum systems in which acoustic resonators couple to superconducting qubits are promising quantum information platforms. High quality factors and small mode volumes make acoustic modes ideal quantum memories, while the qubit-phonon coupling enables the initialization and manipulation of quantum states. We present a scheme for quantum computing with multimode quantum acoustic systems, and based on this scheme, propose a hardware-efficient implementation of a quantum random access memory (qRAM). Quantum information is stored in high-Q phonon modes, and couplings between modes are engineered by applying off-resonant drives to a transmon qubit. In comparison to existing proposals that involve directly exciting the qubit, this scheme can offer a substantial improvement in gate fidelity for long-lived acoustic modes. We show how these engineered phonon-phonon couplings can be used to access data in superposition according to the state of designated address modes—implementing a qRAM on a single chip.

**Introduction.**—The coupling of superconducting qubits to microwave resonators, termed circuit quantum electrodynamics (cQED) [1, 2], constitutes one of today’s most promising quantum computing architectures. Microwave modes provide good quantum memories [3], while superconducting nonlinearities enable the initialization [4], manipulation [5, 6], readout [7], and protection [8, 9] of quantum states encoded in microwave photons. However, long microwave wavelengths pose a potential limitation to the scalability of cQED systems. On-chip resonators face trade-offs between compactness and quality factor [10, 11], and microwave modes with millisecond coherence or better have thus far only been demonstrated in large 3D cavities [3, 12].

Recently, coherent couplings between superconducting qubits and acoustic resonators have been demonstrated in a remarkable series of experiments [13–25]. These so-called circuit quantum acoustodynamic (cQAD) systems (Fig. 1) possess many of the advantageous properties of cQED systems, e.g., superconducting qubits can be used to generate arbitrary superpositions of acoustic Fock states [17, 21], and phonon-number resolving measurements can be performed in the dispersive regime [24, 25]. Yet relative to electromagnetic modes, acoustic modes can provide dramatic benefits in terms of size and coherence times. The velocities of light and sound differ by five orders of magnitude, and short acoustic wavelengths enable the fabrication of ultra-compact phononic resonators [26]. Furthermore, acoustic modes can be exceptionally well-isolated from their environments—quality factors in excess of  $10^{10}$  were recently demonstrated in GHz frequency phononic crystal resonators [27]. A variety of applications for such platforms have been proposed, including quantum transduction [28], entanglement generation [29, 30], and quantum signal processing [31, 32], but surprisingly the direct use of cQAD systems for quantum computing has received relatively little

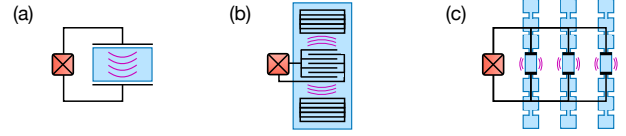


FIG. 1. Hybrid acoustic-superconducting systems for multimode cQAD. A transmon qubit (red) is piezoelectrically coupled to (a) a bulk acoustic wave resonator, (b) a surface acoustic wave resonator, or (c) an array of phononic crystal resonators.

attention, with the notable exception of Ref. [33].

In this work, we propose a hardware-efficient and scalable quantum computing architecture for multimode cQAD systems. Quantum information is stored in high-quality acoustic modes, and interactions between modes are engineered by applying off-resonant drives to an ancillary superconducting transmon qubit. During these operations, the transmon is only virtually excited, so the effects of transmon decoherence are mitigated. This is a crucial property, since the transmon’s decoherence rate can exceed that of the phonons by orders of magnitude. In comparison to existing proposals that involve directly exciting the transmon [33, 34], this virtual approach can offer substantial improvement in gate fidelity for long-lived phonons. This scheme is also directly applicable to multimode cQED systems [34].

Furthermore, to demonstrate the benefits that the proposed cQAD architecture affords in hardware efficiency, we propose an implementation of a quantum random access memory (qRAM) [35, 36]. A classical RAM is a device that can query a database. Given an address  $j$  as input, the RAM outputs the element  $D_j$  stored at position  $j$  in the database. Analogously, a qRAM is a device that, when provided with a superposition of addresses,

returns a correlated superposition of data [37],

$$\sum_{j=1}^N \alpha_j |j\rangle_a |0\rangle_b \xrightarrow{\text{qRAM}} \sum_{j=1}^N \alpha_j |j\rangle_a |D_j\rangle_b, \quad (1)$$

where the subscripts  $a$  and  $b$  denote the address and output qubit registers, respectively. The ability to perform such queries efficiently, i.e. in  $\log N$  time, is a prerequisite for a variety of quantum algorithms that provide speedups over their classical counterparts [38–40]. However, building a qRAM is a highly non-trivial task; even a small-scale qRAM of the sort described in Ref. [35] has yet to be experimentally demonstrated. One major challenge is that, to query a database of size  $N$ , a qRAM requires order  $N$  quantum resources [36]. Hardware-efficiency is thus crucial for qRAM queries of large datasets, and in our implementation this efficiency is enabled by the on-chip integration of superconducting circuits with compact, high-quality acoustic resonators. Our proposal both provides a roadmap for a near-term demonstration of a qRAM, and improves qRAM feasibility in the long term by reducing physical resource requirements.

*Quantum computing in cQAD.*—In multimode cQAD, a transmon qubit is piezoelectrically coupled to a collection of acoustic modes. These modes can be supported in bulk acoustic wave (BAW) [16–18] or surface acoustic wave (SAW) [19–24] resonators, or in an array of phononic crystal (PC) resonators [25] (Fig. 1). Quality factors of  $\approx 10^5$ ,  $10^8$ , and  $10^{10}$  have been measured at GHz frequencies in SAW [41, 42], BAW [43, 44], and PC resonators [27], respectively, and the transmon can be simultaneously coupled to large numbers of high-Q modes on a single chip, even hundreds at once [16]. These systems can be described by the Hamiltonian

$$H = \omega_q q^\dagger q - \frac{\alpha}{2} q^\dagger q^\dagger q q + \sum_k \left( \omega_k m_k^\dagger m_k + g_k q^\dagger m_k + g_k^* q m_k^\dagger \right) + H_d \quad (2)$$

Here,  $q$  and  $m_k$  denote the annihilation operators for the transmon and phonon modes, respectively. The transmon is modeled as an anharmonic oscillator with Kerr nonlinearity  $\alpha$  and is coupled to the  $k^{\text{th}}$  phonon mode with strength  $g_k$  (typically a few MHz [19, 25, 45]). In combination with external drives on the transmon  $H_d = \sum_j \Omega_j q^\dagger e^{-i\omega_j t} + \text{H.c.}$ , this coupling provides the basic tool to initialize, manipulate, and measure phononic qubits [17, 21]. For example, itinerant photon-encoded qubits sent to the system can be routed into a particular phonon mode via pitch-and-catch schemes [46–50].

Interactions between phonon modes can be engineered by applying off-resonant drives to the transmon, and we use these interactions to implement a universal gate set for phononic qubits. The main idea is that the transmon’s Kerr nonlinearity enables it to act as a four-wave mixer [51–54], so phonons can be converted from one frequency to another by driving the transmon. For example,

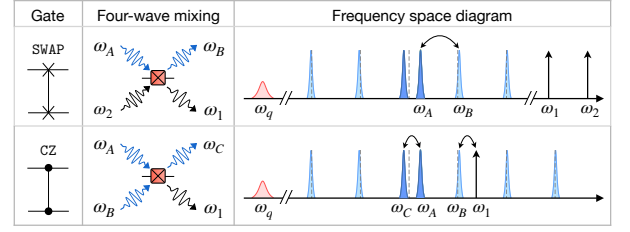


FIG. 2. Inter-phonon gates. **SWAP**: Applying two drives with  $\omega_2 - \omega_1 = \omega_B - \omega_A$  creates an effective coupling between modes  $A$  and  $B$ . **CZ**: Applying a single drive with  $\omega_1 = \omega_A + \omega_B - \omega_C$  creates an effective three-mode coupling between modes  $A$ ,  $B$ , and  $C$ . Frequency shifts of strongly hybridized modes (dark blue) can enable selective coupling when the modes are otherwise uniformly spaced (dashed lines denote uniform spacing) [55].

phonons can be converted from frequency  $\omega_A$  to  $\omega_B$  by applying two drive tones whose frequencies  $\omega_{1,2}$  satisfy the resonance condition  $\omega_2 - \omega_1 = \omega_B - \omega_A$ , see Fig. 2. This driving gives rise to an effective Hamiltonian  $H = g_v^{(1)} m_A m_B^\dagger + \text{H.c.}$ , where  $g_v^{(1)} = -2\alpha \frac{g_A}{\delta_A} \frac{g_B}{\delta_B} \frac{\Omega_1}{\delta_1} \frac{\Omega_2}{\delta_2} (1 - \beta^{(1)})$ . Here,  $\delta_j \equiv \omega_j - \omega_q$ , and  $\beta^{(1)}$  is a correction factor that is significant for strong drives (See the supplementary material [55] for derivations). Evolution under this coupling for a time  $\pi/2g_v^{(1)}$  implements a **SWAP** gate, which exchanges the states of modes  $m_A$  and  $m_B$ , while evolution for a time  $\pi/4g_v^{(1)}$  implements a 50:50 beamsplitter operation [53].

Three-mode interactions can be engineered in a similar fashion (Fig. 2). Applying a single drive tone with frequency  $\omega_1 = \omega_A + \omega_B - \omega_C$  gives rise to the effective Hamiltonian  $H = g_v^{(2)} m_A m_B m_C^\dagger + \text{H.c.}$ , where  $g_v^{(2)} = -2\alpha \frac{g_A}{\delta_A} \frac{g_B}{\delta_B} \frac{g_C}{\delta_C} \frac{\Omega_1}{\delta_1} (1 - \beta^{(2)})$  [55]. This three-mode interaction can be used to implement a controlled phase (**CZ**) gate for qubits encoded in the  $|0, 1\rangle$  phonon Fock states [56]. To perform a **CZ** gate between qubits in modes  $A$  and  $B$ , mode  $C$  is used as an ancilla and initialized in  $|0\rangle$ . Evolving for a time  $\pi/g_v^{(2)}$  then enacts the mapping  $|110\rangle_{ABC} \rightarrow |001\rangle \rightarrow -|110\rangle$ , while leaving all other initial states unaffected. The state  $|11\rangle_{AB}$  acquires a relative geometric phase, thereby implementing the **CZ** gate.

A variety of other operations can be similarly implemented. For example, single- and two-mode squeezing can be implemented by driving the transmon at appropriate frequencies, and phase shifts can be imparted by tuning the relative phase of the drives during **SWAP** operations. Together, these two- and three-mode interactions are sufficient for universal quantum computation [57]. In the remainder of this work, however, we focus on the beamsplitter, **SWAP**, and **CZ** operations, as these are the only operations which we require to implement a qRAM.

It is important to note that in BAW and SAW resonators, phonon mode frequencies are approximately uniformly spaced, i.e.  $\omega_{j+1} - \omega_j = \nu$ , where  $\nu$  is the free spectral range. This uniform spacing can lead to prob-

lematic degeneracies in the resonance conditions above. Nonuniform mode spacing is thus necessary to enable selective coupling, and in [55] we describe several ways to engineer nonuniformity in BAW and SAW systems. As shown in Fig. 2, one approach is to couple the phonons to an external mode, such as a microwave cavity or resonator, so that the resulting hybridization shifts mode frequencies [45]. Nonuniformity can also be realized in composite resonators [58], or by coupling the transmon to two families of phonon modes [18]. In [55], we also introduce a metric,  $\Delta\nu$ , to quantify the nonuniformity. Roughly speaking,  $\Delta\nu$  is the scale at which the mode spacing varies.

**Gate fidelities.**—During the gates described above, the transmon is never directly excited; instead, it is only *virtually* excited, so infidelity attributable to transmon decoherence is suppressed. These virtual gates can thus provide great advantage in cQAD systems, where transmon decoherence is likely to be the limiting factor. This is in contrast to existing proposals [33, 34], in which gates between resonator mode qubits are implemented by swapping information *directly* into the transmon using resonant interactions of the form  $g_d(q^\dagger m + qm^\dagger)$ , which can be engineered, e.g., by modulating the transmon's frequency. In the following, we compare the predicted fidelities of the *virtual* gates proposed here and the *direct* gates considered in Refs. [33, 34].

In a multimode architecture, there exists a fundamental tradeoff between decoherence and spectral crowding. Slower gates are more prone to decoherence, while faster gates have reduced frequency resolution and can disrupt other modes. The infidelities of the direct and virtual gates, respectively  $1 - \mathcal{F}_d$  and  $1 - \mathcal{F}_v$ , can be approximated as a sum of contributions from these two effects [33],

$$1 - \mathcal{F}_d \approx c_d \left[ \frac{\kappa + \gamma}{2} \frac{\pi}{2g_d} + \left( \frac{g_d}{\nu} \right)^2 \right], \quad (3)$$

$$1 - \mathcal{F}_v \approx c_v \left[ \bar{\kappa}_\gamma \frac{\pi}{2g_v} + \left( \frac{g_v}{\Delta\nu} \right)^2 \right], \quad (4)$$

where  $\kappa$  and  $\gamma$  are the bare phonon and transmon decoherence rates, and  $c_{d,v}$  are constants accounting for the durations of each gate ( $c_v = 1$  for SWAP, and  $c_v = 2$  for CZ, as these gates have durations  $\pi/2g_v$  and  $\pi/g_v$  respectively. As discussed in Ref. [34],  $c_d = 5$  for SWAP and  $c_d = 4$  for CZ.)

The first terms in Eq. (3) and Eq. (4) account for decoherence. During direct gates, information spends roughly equal time in the phonon and transmon modes, so the average decoherence rate is  $(\kappa + \gamma)/2$ . During virtual gates, the average decoherence rate,  $\bar{\kappa}_\gamma$ , is  $\bar{\kappa}_\gamma = (\kappa_\gamma^A + \kappa_\gamma^B)/2$  for SWAP, and  $\bar{\kappa}_\gamma = (\kappa_\gamma^A + \kappa_\gamma^B + \kappa_\gamma^C)/2$  for CZ. Here,  $\kappa_\gamma^j = \kappa + \gamma(g_j/\delta_j)^2(1 + \beta^{(\gamma)})$  denotes the dressed decay rate of mode  $j$ , which includes a contribution from the inverse Purcell effect [3, 54] and a drive-dependent correction  $\beta^{(\gamma)}$  [55]. The second term in each expression accounts for spectral crowding. The probability of accidentally exciting another mode scales as  $(g_d/\nu)^2$  in the

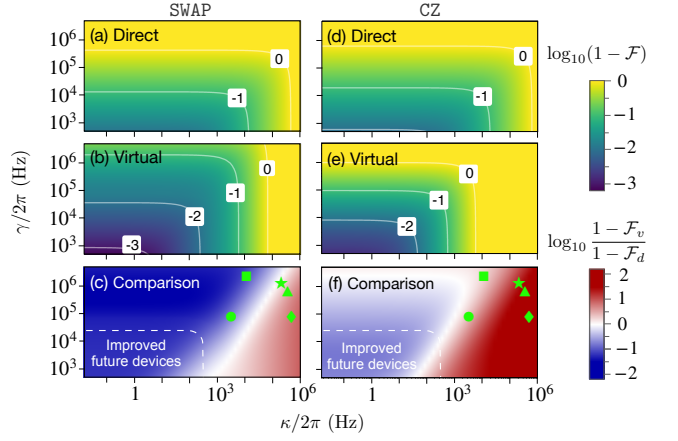


FIG. 3. Comparison of direct and virtual operations. (a,b)  $\log_{10}(1 - \mathcal{F})$  for the direct and virtual SWAP operations, respectively. The couplings are optimized subject to constraints ( $g_d \in [0, g]$ , constraints on  $g_v$  are discussed in [55]). (c) Comparison of direct and virtual SWAP operations. The log ratio of the infidelities is plotted, with the virtual operations attaining higher fidelities in the blue region. (d,e)  $\log_{10}$  infidelity for the direct and virtual CZ operations. (f) Comparison of CZ operations. For reference, the symbols  $\{\bullet, \blacksquare, \blacktriangle, \blacklozenge, \star\}$  respectively denote the  $\kappa$  and  $\gamma$  values measured in Refs. [17], [19], [25], [21], and [22]. Note, however, that the plots are generated using typical parameter values, not specific values from any one experiment. Parameters for all plots:  $g/2\pi = 10\text{MHz}$ ,  $\delta/2\pi = 100\text{MHz}$ ,  $\nu/2\pi = 10\text{MHz}$ , and  $\Delta\nu/2\pi = 1\text{MHz}$ .

direct case, and as  $(g_v/\Delta\nu)^2$  in the virtual case.

The competition between decoherence and spectral crowding results in an optimal coupling rate [33]. The couplings  $g_{d,v}$  can be tuned to reach their optima either by changing the modulation amplitude in the direct case [34], or by changing the drive strengths in the virtual case. At their respective optima, the infidelities are

$$1 - \mathcal{F}_d \approx \frac{3c_d}{2} \left[ \frac{\pi(\kappa + \gamma)}{2\sqrt{2}\nu} \right]^{2/3}, \quad (5)$$

$$1 - \mathcal{F}_v \approx \frac{3c_v}{2} \left[ \frac{\pi\bar{\kappa}_\gamma}{\sqrt{2}\Delta\nu} \right]^{2/3}. \quad (6)$$

While transmon and phonon decoherence contribute equally to  $1 - \mathcal{F}_d$ , transmon decoherence only makes a small contribution to  $1 - \mathcal{F}_v$  via the inverse Purcell effect, wherein  $\gamma$  is suppressed by a factor of  $(g/\delta)^2 \ll 1$ . The virtual gates can thus be expected to attain higher fidelities when there is a large disparity between  $\gamma$  and  $\kappa$ , i.e. for sufficiently long-lived phonon modes. Indeed,  $\mathcal{F}_v > \mathcal{F}_d$  whenever  $\kappa_\gamma \lesssim (\kappa + \gamma)\Delta\nu/\nu$ , provided the optimal coupling rates can be reached.

In Fig. 3, we plot the optimal infidelities of direct and virtual gates as a function of  $\kappa$  and  $\gamma$  for currently feasible experimental parameters. The comparison reveals that virtual gates can be performed with high fidelity ( $>99\%$ ) given long-lived phonons, and that virtual gates attain

higher fidelities than direct gates in the same regime. Indeed, realistic improvements in phonon coherence are likely to bring near-term devices into this  $\mathcal{F}_v \gg \mathcal{F}_d$  regime (Fig. 3c,f).

We briefly note other factors relevant to the comparison of direct and virtual gates. *Multi-phonon encodings.* Direct gates require that qubits be encoded in the  $|0,1\rangle$  phonon Fock states, while virtual operations are compatible with multi-phonon encodings, including some bosonic quantum error-correcting codes [57, 59]. *Parallelism.* Direct gates must be executed serially, while virtual gates can be executed in parallel by simultaneously applying the requisite drives (though care should be taken to ensure that the additional drives do not bring spurious couplings on resonance). *Speed.* Virtual gates are inherently slower than direct gates, with realistically attainable virtual coupling rates on the order of  $g_v/2\pi \sim 10 - 100$  kHz [55].

*qRAM Implementation.*—To illustrate the advantages of cQAD systems, we propose an implementation of a qRAM [35, 36]. As defined by Eq.(1), a qRAM is a device which can query a database with an address in superposition. The ability to perform such queries efficiently is a prerequisite for a variety of quantum algorithms, including Grover’s search [38, 60] matrix inversion [39], and various proposals in the field of quantum machine learning [40]. While demanding hardware and connectivity requirements have thus far precluded an experimental demonstration of a qRAM, our proposed cQAD implementation is naturally hardware-efficient. Indeed, a small-scale cQAD qRAM can be implemented with just a single multimode resonator.

The elementary building block of our qRAM implementation is a *quantum router*, shown in Fig. 4(a). The router directs an incoming qubit into different output modes conditioned on the state of a routing qubit. When the routing qubit is in state  $|0\rangle$  ( $|1\rangle$ ), an incoming qubit  $|\psi\rangle$  in the top mode is swapped to the left(right) mode. The routers are implemented using the operations described above: the routing circuit contains a **SWAP** and a controlled-**SWAP** gate, the latter of which is implemented using **CZ** and beamsplitter operations (Fig. 4b).

To implement a qRAM, a collection of routers is arranged in a binary tree, with the outputs of routers at one level acting as inputs to routers at the next (Fig. 4c). To query the database at the bottom of the tree, qubits from the address register are routed sequentially into the tree, with earlier address qubits controlling the routing of later ones in a “bucket-brigade” scheme [35]. A so-called bus qubit then follows the path paved by the address qubits and extracts the data, after which it is routed back out of the tree and into the output register. Finally, to disentangle the address and routers, the address qubits are routed back out of the tree. Since all routing operations are quantum-controlled, preparing the address register in superposition allows access to the data in superposition, thereby implementing operation (1). Further details are provided in [55].

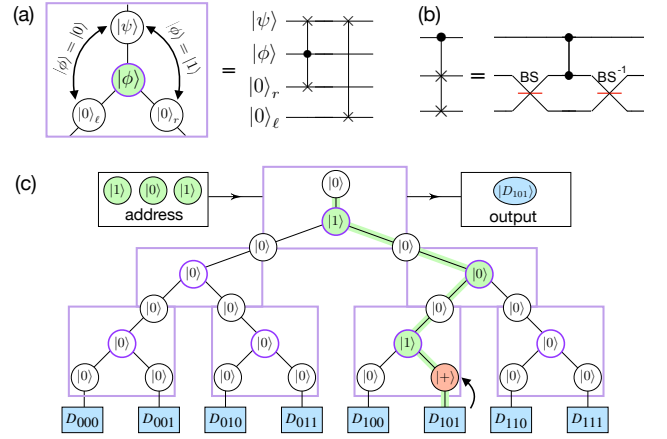


FIG. 4. cQAD implementation of qRAM. (a) Quantum router. Each circle represents a phonon mode. The router directs the qubit  $|\psi\rangle$  in the incoming mode (top) to either the right or left mode conditioned on the state of the routing qubit  $|\phi\rangle$ . (b) Realization of a controlled **SWAP** gate with beamsplitter and **CZ** operations. (c) qRAM implementation. Address qubits (green) are routed into position one-by-one, carving out a path to the database. The bus qubit (red) follows this path to retrieve the data  $D_j$ . The bus and address qubits are then routed back out of the tree to complete the query. The database (blue squares) can be either classical or quantum. In the former case, the bus is initially prepared in  $|+\rangle$ , and classical bits are copied to the bus by applying phase shifts to each mode at the bottom of the tree. In the latter case, the data qubit is extracted through a sequence of controlled **SWAP** operations. See [55] for details.

We highlight three appealing properties of this cQAD-based qRAM.

1. *Hardware-efficiency.* Hundreds of phonon modes can simultaneously couple to a transmon on a single chip [16]. Thus, the hardware and fabrication cost of a cQAD-based qRAM can be drastically reduced in comparison to cavity- [36] or circuit-QED [61] implementations.
2. *Scalability.* It is not necessary to control all routing through a single transmon; since only adjacent routers are coupled (Fig. 4c), different regions of the tree can be controlled and implemented independently. For example, the qRAM can be built out of several modules, where each module comprises a group of routers controlled by a single transmon. The phononic modes in each module could be supported in physically separate resonators, or multiple transmons could be simultaneously coupled to the same multimode resonator to give access to a large bandwidth of modes, potentially spanning several GHz [16].
3. *Error resilience.* Because our implementation follows the bucket-brigade model, it inherits a favorable  $\log N$  error scaling [35, 36, 62]. In particular, the scaling argument of Ref. [35] directly applies to the case of phonon-loss errors: the query infidelity scales as  $1 - \mathcal{F} \sim \varepsilon \log N$ , where  $\varepsilon$  is the phonon loss probability. Remarkably, one can show that the infidelity scales logarithmically



for arbitrary independent, incoherent errors [63], such as phonon loss, dephasing, and heating.

*Discussion.*—We have proposed a quantum computing architecture for multimode cQAD and an implementation of a qRAM based on it. The implementation is hardware-efficient, owing to the compactness of multimode cQAD systems that is enabled by small acoustic wavelengths. We emphasize that hardware efficiency is not only crucial for scaling to large system sizes, but that it is also particularly advantageous for near-term experiments. Indeed, a small-scale qRAM can be implemented even with just a single multimode resonator. In the long term, the use of bosonic quantum error correcting codes [59, 64] and compatible logical gates [57, 65, 66] to implement a qRAM that is both fault-tolerant and hardware-efficient is an intriguing direction for future research. We note that these ideas can also be directly applied to multimode cQED.

To be viable, our scheme requires long phonon coherence times ( $1/\kappa \gg 1/g_v$ ). Though loss due to intrinsic material processes like phonon-phonon scattering or two level systems limit phonon coherence, such mechanisms should not prevent access to this regime. For

example, both BAW and PC quality factors can approach  $10^{10}$  before encountering limits posed by intrinsic mechanisms [27, 67, 68], corresponding to  $\kappa/2\pi \sim 1$  Hz at GHz frequencies, while  $g_v/2\pi \sim 10 - 100$  kHz is realistically attainable. Additionally, intrinsic sources of phonon dephasing are not expected [69]. Phonon decoherence in current cQAD experiments is thus likely dominated by extrinsic mechanisms that can be mitigated with improved fabrication techniques, though the extent to which the coupling to superconducting circuits may limit phonon coherence in cQAD is an important open question.

*Acknowledgements.*—We thank Vijay Jain, Prashanta Kharel, Patricio Arrangoiz-Arriola, Alex Wollack, Hong Tang, Peter Rakich, and Oskar Painter for helpful discussions. C.T.H. acknowledges support from the NSF Graduate Research Fellowship Program (DGE1752134). We acknowledge support from the ARL-CDQI (W911NF-15-2-0067, W911NF-18-2-0237), ARO (W911NF-18-1-0020, W911NF-18-1-0212), ARO MURI (W911NF-16-1-0349), AFOSR MURI (FA9550-15-1-0015), DOE (DE-SC0019406), NSF (EFMA-1640959, DMR-1609326), and the Packard Foundation (2013-39273).

- 
- [1] A. Blais, J. Gambetta, A. Wallraff, D. I. Schuster, S. M. Girvin, M. H. Devoret, and R. J. Schoelkopf, *Phys. Rev. A* **75**, 032329 (2007).
  - [2] R. J. Schoelkopf and S. M. Girvin, *Nature* **451**, 664 (2008).
  - [3] M. Reagor, W. Pfaff, C. Axline, R. W. Heeres, N. Ofek, K. Sliwa, E. Holland, C. Wang, J. Blumoff, K. Chou, M. J. Hatridge, L. Frunzio, M. H. Devoret, L. Jiang, and R. J. Schoelkopf, *Phys. Rev. B* **94**, 014506 (2016).
  - [4] M. Hofheinz, E. M. Weig, M. Ansmann, R. C. Bialczak, E. Lucero, M. Neeley, A. D. O’Connell, H. Wang, J. M. Martinis, and A. N. Cleland, *Nature* **454**, 310 (2008).
  - [5] S. Krastanov, V. V. Albert, C. Shen, C.-L. Zou, R. W. Heeres, B. Vlastakis, R. J. Schoelkopf, and L. Jiang, *Phys. Rev. A* **92**, 040303 (2015).
  - [6] R. W. Heeres, P. Reinhold, N. Ofek, L. Frunzio, L. Jiang, M. H. Devoret, and R. J. Schoelkopf, *Nat. Commun.* **8**, 94 (2017).
  - [7] L. Sun, A. Petrenko, Z. Leghtas, B. Vlastakis, G. Kirchmair, K. M. Sliwa, A. Narla, M. Hatridge, S. Shankar, J. Blumoff, L. Frunzio, M. Mirrahimi, M. H. Devoret, and R. J. Schoelkopf, *Nature* **511**, 444 (2014).
  - [8] N. Ofek, A. Petrenko, R. Heeres, P. Reinhold, Z. Leghtas, B. Vlastakis, Y. Liu, L. Frunzio, S. M. Girvin, L. Jiang, M. Mirrahimi, M. H. Devoret, and R. J. Schoelkopf, *Nature* **536**, 441 (2016).
  - [9] L. Hu, Y. Ma, W. Cai, X. Mu, Y. Xu, W. Wang, Y. Wu, H. Wang, Y. P. Song, C.-L. Zou, S. M. Girvin, L.-M. Duan, and L. Sun, *Nat. Phys.* **15**, 503 (2019).
  - [10] K. Geerlings, S. Shankar, E. Edwards, L. Frunzio, R. J. Schoelkopf, and M. H. Devoret, *Appl. Phys. Lett.* **100**, 192601 (2012).
  - [11] J. Wenner, R. Barends, R. C. Bialczak, Y. Chen, J. Kelly, E. Lucero, M. Mariantoni, A. Megrant, P. J. J. O’Malley, D. Sank, A. Vainsencher, H. Wang, T. C. White, Y. Yin, J. Zhao, A. N. Cleland, and J. M. Martinis, *Appl. Phys. Lett.* **99**, 113513 (2011).
  - [12] A. Romanenko, R. Pilipenko, S. Zorzetti, D. Frolov, M. Awida, S. Posen, and A. Grassellino, *arXiv:1810.03703*.
  - [13] A. D. O’Connell, M. Hofheinz, M. Ansmann, R. C. Bialczak, M. Lenander, E. Lucero, M. Neeley, D. Sank, H. Wang, M. Weides, J. Wenner, J. M. Martinis, and A. N. Cleland, *Nature* **464**, 697 (2010).
  - [14] J.-M. Pirkkalainen, S. U. Cho, J. Li, G. S. Paraoanu, P. J. Hakonen, and M. A. Sillanpää, *Nature* **494**, 211 (2013).
  - [15] M. V. Gustafsson, T. Aref, A. F. Kockum, M. K. Ekström, G. Johansson, and P. Delsing, *Science* **346**, 207 (2014).
  - [16] Y. Chu, P. Kharel, W. H. Renninger, L. D. Burkhardt, L. Frunzio, P. T. Rakich, and R. J. Schoelkopf, *Science* **358**, 199 (2017).
  - [17] Y. Chu, P. Kharel, T. Yoon, L. Frunzio, P. T. Rakich, and R. J. Schoelkopf, *Nature* **563**, 666 (2018).
  - [18] M. Kervinen, I. Rissanen, and M. Sillanpää, *Phys. Rev. B* **97**, 205443 (2018).
  - [19] R. Manenti, A. F. Kockum, A. Patterson, T. Behrle, J. Rahamim, G. Tancredi, F. Nori, and P. J. Leek, *Nat. Commun.* **8**, 975 (2017).
  - [20] A. Noguchi, R. Yamazaki, Y. Tabuchi, and Y. Nakamura, *Phys. Rev. Lett.* **119**, 180505 (2017).
  - [21] K. J. Satzinger, Y. P. Zhong, H.-S. Chang, G. A. Peairs, A. Bienfait, M.-H. Chou, A. Y. Cleland, C. R. Conner, É. Dumur, J. Grebel, I. Gutierrez, B. H. November, R. G. Povey, S. J. Whiteley, D. D. Awschalom, D. I. Schuster, and A. N. Cleland, *Nature* **563**, 661 (2018).
  - [22] B. A. Moores, L. R. Sletten, J. J. Viennot, and K. W.

- Lehnert, Phys. Rev. Lett. **120**, 227701 (2018).
- [23] A. N. Bolgar, J. I. Zotova, D. D. Kirichenko, I. S. Besedin, A. V. Semenov, R. S. Shaikhaidarov, and O. V. Astafiev, Phys. Rev. Lett. **120**, 223603 (2018).
- [24] L. R. Sletten, B. A. Moores, J. J. Viennot, and K. W. Lehnert, Phys. Rev. X **9**, 021056 (2019).
- [25] P. Arrangoiz-Arriola, E. A. Wollack, Z. Wang, M. Pechal, W. Jiang, T. P. McKenna, J. D. Witmer, and A. H. Safavi-Naeini, arXiv:1902.04681.
- [26] A. H. Safavi-Naeini, D. V. Thourhout, R. Baets, and R. V. Laer, Optica **6**, 213 (2019).
- [27] G. S. MacCabe, H. Ren, J. Luo, J. D. Cohen, H. Zhou, A. Sipahigil, M. Mirhosseini, and O. Painter, arXiv:1901.04129.
- [28] M. J. A. Schuetz, E. M. Kessler, G. Giedke, L. M. K. Vandersypen, M. D. Lukin, and J. I. Cirac, Phys. Rev. X **5**, 031031 (2015).
- [29] A. N. Cleland and M. R. Geller, Phys. Rev. Lett. **93**, 070501 (2004).
- [30] A. Bienfait, K. J. Satzinger, Y. P. Zhong, H.-S. Chang, M.-H. Chou, C. R. Conner, É. Dumur, J. Grebel, G. A. Peairs, R. G. Povey, and A. N. Cleland, Science **364**, 368 (2019).
- [31] L. Guo, A. Grimsmo, A. F. Kockum, M. Pletyukhov, and G. Johansson, Phys. Rev. A **95**, 053821 (2017).
- [32] G. Andersson, B. Suri, L. Guo, T. Aref, and P. Delsing, arXiv:1812.01302.
- [33] M. Pechal, P. Arrangoiz-Arriola, and A. H. Safavi-Naeini, Quantum Sci. Technol. **4**, 015006 (2018).
- [34] R. K. Naik, N. Leung, S. Chakram, P. Groszkowski, Y. Lu, N. Earnest, D. C. McKay, J. Koch, and D. I. Schuster, Nat. Commun. **8**, 1904 (2017).
- [35] V. Giovannetti, S. Lloyd, and L. Maccone, Phys. Rev. Lett. **100**, 160501 (2008).
- [36] V. Giovannetti, S. Lloyd, and L. Maccone, Phys. Rev. A **78**, 052310 (2008).
- [37] We reserve the term qRAM for a device which can perform operation (1). This term should not be confused with the idea of a random access quantum memory (RAQM)—a memory in which qubits can be stored and retrieved in any order [70, 71].
- [38] L. K. Grover, Phys. Rev. Lett. **79**, 325 (1997).
- [39] A. W. Harrow, A. Hassidim, and S. Lloyd, Phys. Rev. Lett. **103**, 150502 (2009).
- [40] J. Biamonte, P. Wittek, N. Pancotti, P. Rebentrost, N. Wiebe, and S. Lloyd, Nature **549**, 195 (2017).
- [41] R. Manenti, M. J. Peterer, A. Nersisyan, E. B. Magnusson, A. Patterson, and P. J. Leek, Phys. Rev. B **93**, 041411 (2016).
- [42] T. Aref, P. Delsing, M. K. Ekström, A. F. Kockum, M. V. Gustafsson, G. Johansson, P. J. Leek, E. Magnusson, and R. Manenti, in *Superconducting Devices in Quantum Optics*, edited by R. H. Hadfield and G. Johansson (Springer International Publishing, Cham, 2016) pp. 217–244.
- [43] W. H. Renninger, P. Kharel, R. O. Behunin, and P. T. Rakich, Nat. Phys. **14**, 601 (2018).
- [44] P. Kharel, Y. Chu, M. Power, W. H. Renninger, R. J. Schoelkopf, and P. T. Rakich, APL Photonics **3**, 066101 (2018).
- [45] X. Han, C.-L. Zou, and H. X. Tang, Phys. Rev. Lett. **117**, 123603 (2016).
- [46] T. A. Palomaki, J. W. Harlow, J. D. Teufel, R. W. Simmonds, and K. W. Lehnert, Nature **495**, 210 (2013).
- [47] M. Pechal, L. Huthmacher, C. Eichler, S. Zeytinoglu, A. A. Abdumalikov, S. Berger, A. Wallraff, and S. Filipp, Phys. Rev. X **4**, 041010 (2014).
- [48] S. J. Srinivasan, N. M. Sundaresan, D. Sadri, Y. Liu, J. M. Gambetta, T. Yu, S. M. Girvin, and A. A. Houck, Phys. Rev. A **89**, 033857 (2014).
- [49] C. J. Axline, L. D. Burkhardt, W. Pfaff, M. Zhang, K. Chou, P. Campagne-Ibarcq, P. Reinhold, L. Frunzio, S. M. Girvin, L. Jiang, M. H. Devoret, and R. J. Schoelkopf, Nat. Phys. **14**, 705 (2018).
- [50] P. Kurpiers, P. Magnard, T. Walter, B. Royer, M. Pechal, J. Heinsoo, Y. Salathé, A. Akin, S. Storz, J.-C. Besse, S. Gasparinetti, A. Blais, and A. Wallraff, Nature **558**, 264 (2018).
- [51] J. Y. Mutus, T. C. White, E. Jeffrey, D. Sank, R. Barends, J. Bochmann, Y. Chen, Z. Chen, B. Chiaro, A. Dunsworth, J. Kelly, A. Megrant, C. Neill, P. J. J. O’Malley, P. Roushan, A. Vainsencher, J. Wenner, I. Siddiqi, R. Vijay, A. N. Cleland, and J. M. Martinis, Appl Phys Lett **103**, 122602 (2013).
- [52] Z. Leghtas, S. Touzard, I. M. Pop, A. Kou, B. Vlastakis, A. Petrenko, K. M. Sliwa, A. Narla, S. Shankar, M. J. Hatridge, M. Reagor, L. Frunzio, R. J. Schoelkopf, M. Mirrahimi, and M. H. Devoret, Science **347**, 853 (2015).
- [53] Y. Y. Gao, B. J. Lester, Y. Zhang, C. Wang, S. Rosenblum, L. Frunzio, L. Jiang, S. M. Girvin, and R. J. Schoelkopf, Phys. Rev. X **8**, 021073 (2018).
- [54] Y. Zhang, B. J. Lester, Y. Y. Gao, L. Jiang, R. J. Schoelkopf, and S. M. Girvin, Phys. Rev. A **99**, 012314 (2019).
- [55] See Supplementary Material.
- [56] N. K. Langford, S. Ramelow, R. Prevedel, W. J. Munro, G. J. Milburn, and A. Zeilinger, Nature **478**, 360 (2011).
- [57] M. Y. Niu, I. L. Chuang, and J. H. Shapiro, Phys. Rev. Lett. **120**, 160502 (2018).
- [58] P. Kharel, G. I. Harris, E. A. Kittlaus, W. H. Renninger, N. T. Otterstrom, J. G. E. Harris, and P. T. Rakich, arXiv:1809.04020.
- [59] M. Y. Niu, I. L. Chuang, and J. H. Shapiro, Phys. Rev. A **97**, 032323 (2018).
- [60] Quantum error correction will likely be necessary for algorithms that require super-polynomially many qRAM queries [62].
- [61] T. H. Kyaw, S. Felicetti, G. Romero, E. Solano, and L.-C. Kwek, Sci. Rep. **5**, 8621 (2015).
- [62] S. Arunachalam, V. Gheorghiu, T. Jochym-O’Connor, M. Mosca, and P. V. Srinivasan, New J. Phys. **17**, 123010 (2015).
- [63] C. T. Hann and L. Jiang, (in preparation).
- [64] V. V. Albert, K. Noh, K. Duivenvoorden, D. J. Young, R. T. Brierley, P. Reinhold, C. Vuillot, L. Li, C. Shen, S. M. Girvin, B. M. Terhal, and L. Jiang, Phys. Rev. A **97**, 032346 (2018).
- [65] H. K. Lau and M. B. Plenio, Phys Rev Lett **117**, 100501 (2016).
- [66] Y. Y. Gao, B. J. Lester, K. S. Chou, L. Frunzio, M. H. Devoret, L. Jiang, S. M. Girvin, and R. J. Schoelkopf, Nature **566**, 509 (2019).
- [67] M. Goryachev, D. L. Creedon, E. N. Ivanov, S. Gallioui, R. Bourquin, and M. E. Tobar, Appl. Phys. Lett. **100**, 243504 (2012).
- [68] S. Gallioui, M. Goryachev, R. Bourquin, P. Abbé, J. P.

- Aubry, and M. E. Tobar, *Sci. Rep.* **3**, 2132 (2013).
- [69] T. Faust, J. Rieger, M. J. Seitner, J. P. Kotthaus, and E. M. Weig, *Nat. Phys.* **9**, 485 (2013).
- [70] M. Mariantoni, H. Wang, T. Yamamoto, M. Neeley, R. C. Bialczak, Y. Chen, M. Lenander, E. Lucero, A. D. O'Connell, D. Sank, M. Weides, J. Wenner, Y. Yin, J. Zhao, A. N. Korotkov, A. N. Cleland, and J. M. Martinis, *Science* **334**, 61 (2011).
- [71] N. Jiang, Y.-F. Pu, W. Chang, C. Li, S. Zhang, and L.-M. Duan, *Npj Quantum Inf.* **5**, 28 (2019).
- [72] S. E. Nigg, H. Paik, B. Vlastakis, G. Kirchmair, S. Shankar, L. Frunzio, M. H. Devoret, R. J. Schoelkopf, and S. M. Girvin, *Phys. Rev. Lett.* **108**, 240502 (2012).
- [73] In this section we consider the case  $\omega_A < \omega_B < \omega_1 < \omega_C$ , which nicely highlights the similarities between  $g_v^{(1)}$  and  $g_v^{(2)}$ . The derivations proceed analogously for other cases, such as the case of  $\omega_C < \omega_A < \omega_B < \omega_1$  shown in Fig. 2 of the main text.
- [74] This equation determines  $S$  implicitly; to leading order in the drives,  $S = -2\alpha \sum_j |\Omega_j|^2 / \delta_j^2$ . However, the Hamiltonian (S4) contains the terms  $(\alpha \xi_{1,2} q^{\dagger 2} q e^{-i\delta_{1,2}t} + \text{H.c.})$ , which also contribute to  $S$  at this order. Employing perturbation theory, one finds  $S = -2\alpha \sum_j |\Omega_j|^2 / \delta_j (\delta_j + \alpha)$ , which matches the leading order calculation in Ref. [54]. This latter expression is used in the numerics throughout this work.
- [75] At least two modes from any three come from the same family, and since the modes in each family are uniformly spaced, there necessarily exists another set with the same resonance condition.
- [76] Because SAW resonators have finite bandwidth, care should be taken to avoid coupling to unconfined modes. This problem can be solved in general by engineering the transmon-phonon coupling bandwidth to lie within the SAW resonator bandwidth. The size of both bands can be tuned by varying the number of fingers in the respective interdigitated transducers.
- [77] C. Axline, M. Reagor, R. Heeres, P. Reinhold, C. Wang, K. Shain, W. Pfaff, Y. Chu, L. Frunzio, and R. J. Schoelkopf, *Appl. Phys. Lett.* **109**, 042601 (2016).
- [78] R. Babbush, C. Gidney, D. W. Berry, N. Wiebe, J. McClean, A. Paler, A. Fowler, and H. Neven, *Phys. Rev. X* **8**, 041015 (2018), arXiv:1805.03662.
- [79] S. Chakraborty, A. Gilyén, and S. Jeffery, arXiv:1804.01973.
- [80] A. Gilyén, Y. Su, G. H. Low, and N. Wiebe, arXiv:1806.01838.
- [81] Writing either classical or quantum data to the database generally leaves the database in a superposition, unless entries are written one by one.

## Supplemental Material: Hardware-efficient quantum random access memory with hybrid quantum acoustic systems

### CONTENTS

I. Virtual coupling rates	7
A. Derivation of the virtual coupling rates	8
B. Corrections to the virtual coupling rates	8
C. Comparison with numerical Floquet calculation	9
II. Engineering nonuniform mode spacing	11
A. External mode hybridization	12
B. Two phonon mode families	12
C. Composite resonators	13
D. Example schematics	13
III. Detailed description of the cQAD qRAM	14
A. Operation of a quantum router	14
B. Database access schemes	14

### I. VIRTUAL COUPLING RATES

In this section, we study the virtual coupling rates

$$g_v^{(1)} = -2\alpha \xi_1^* \xi_2 \lambda_A \lambda_B^* (1 - \beta^{(1)}), \quad (\text{S1})$$

$$g_v^{(2)} = -2\alpha \xi_1^* \lambda_A \lambda_B^* \lambda_C (1 - \beta^{(2)}). \quad (\text{S2})$$

Below, we define the notation, derive these expressions, and discuss the importance of the corrections  $\beta^{(1,2)}$  for cQAD systems. Then, in order to verify the accuracy of these expressions, we compare them to numerical results obtained using the Floquet theory methods of Ref. [54].

### A. Derivation of the virtual coupling rates

To derive the expressions (S1) and (S2), we begin with the multimode cQAD Hamiltonian (Eq. 2 of the main text) and perform a unitary transformation defined by  $U_1 = \exp iH_0 t$ , where  $H_0 = \omega_q q^\dagger q + \sum_k \omega_k m_k^\dagger m_k$ . Thus,

$$H = \sum_j (\Omega_j q^\dagger e^{-i\delta_j t} + \text{H.c.}) + \sum_k (g_k m_k q^\dagger e^{-i\delta_k t} + \text{H.c.}) - \frac{\alpha}{2} q^\dagger q^\dagger q q, \quad (\text{S3})$$

where  $\delta_k = \omega_k - \omega_q$  is the detuning of the  $k^{\text{th}}$  phonon mode, while  $\delta_j = \omega_j - \omega_q$  and  $\Omega_j$  are the detuning and the strength of the  $j^{\text{th}}$  drive tone, respectively. In the spirit of Ref. [72], we first perform unitary transformations to eliminate the qubit-phonon couplings and drive terms then consider the effects of the anharmonicity. For notational convenience, we introduce the dimensionless parameters  $\lambda_k \equiv g_k/\delta_k$  and  $\xi_j \equiv \Omega_j/\delta_j$ . To leading order in  $\lambda_k \ll 1$ , the unitary that eliminates the couplings is  $U_2 = \exp \sum_k (\lambda_k^* m_k^\dagger q e^{i\delta_k t} - \text{H.c.})$ , and that which eliminates the drives is  $U_3 = \exp \sum_j (\xi_j^* q e^{i\delta_j t} - \text{H.c.})$ . The combined effect of these two transformations is to enact the mapping  $q \rightarrow q + \sum_j \xi_j e^{-i\delta_j t} + \sum_k \lambda_k m_k e^{-i\delta_k t} \equiv Q$ , so that the Hamiltonian becomes

$$H = -\frac{\alpha}{2} Q^\dagger Q^\dagger Q Q. \quad (\text{S4})$$

Note that we have neglected linear terms of the form  $(\Omega_j^* \lambda_k m_k e^{i(\delta_j - \delta_k)t} + \text{H.c.})$ . This omission is justified in the RWA provided that  $|\delta_j - \delta_k| \gg \lambda_k \Omega_j$ , i.e. that the drives are sufficiently far detuned from any modes in which we are interested. We also neglect frequency (Stark) shifts of the phononic eigenmodes—their only effect is to modify the resonance conditions below.

When two drive tones are applied whose frequencies satisfy the resonance condition  $\omega_2 - \omega_1 = \omega_B - \omega_A$ , the Hamiltonian (S4) contains a resonant beamsplitter-type coupling,  $g_v^{(1)} m_A m_B^\dagger + \text{H.c.}$ , where

$$g_v^{(1)} = -2\alpha \xi_1^* \xi_2 \lambda_A \lambda_B^*. \quad (\text{S5})$$

Similarly, when a single drive tone is applied with frequency  $\omega_1 = \omega_A + \omega_C - \omega_B$  [73], the Hamiltonian contains a resonant three-mode coupling  $g_v^{(2)} m_A m_B^\dagger m_C + \text{H.c.}$ , where

$$g_v^{(2)} = -2\alpha \xi_1^* \lambda_A \lambda_B^* \lambda_C. \quad (\text{S6})$$

### B. Corrections to the virtual coupling rates

The Hamiltonian (S4) contains many terms beyond just the resonant terms discussed above (see Table I). Most of these terms are rapidly-rotating and can be neglected in the RWA assuming dispersive coupling ( $\lambda \ll 1$ ) and weak drives ( $\xi \ll 1$ ). However, other terms can produce corrections  $\beta^{(1,2)}$  to the coupling rates. In this section, we first calculate these corrections to leading order in  $\lambda$  and  $\xi$ . Then, we derive nonperturbative contributions associated with the AC Stark shift.

TABLE I. Catalog of terms in the Hamiltonian (S4). Summations run over all drives and all modes, including the transmon mode  $q$ , for which  $\lambda_q = 1$  and  $\delta_q = 0$ .

Term	Description
$\frac{\alpha}{2} \sum_{i,j,k,l} \xi_i^* \xi_j^* \xi_k \lambda_l m_l e^{i(\delta_i + \delta_j - \delta_k - \delta_l)t} + \text{H.c.}$	Drive
$\frac{\alpha}{2} \sum_{i,j,k,l} \xi_i^* \xi_j \lambda_k^* \lambda_l m_k^\dagger m_l e^{i(\delta_i - \delta_j + \delta_k - \delta_l)t} + \text{H.c.}$	Beamsplitter
$\frac{\alpha}{2} \sum_{i,j,k,l} \xi_i^* \xi_j^* \lambda_k \lambda_l m_k m_l e^{i(\delta_i + \delta_j - \delta_k - \delta_l)t} + \text{H.c.}$	Two-mode squeezing
$\frac{\alpha}{2} \sum_{i,j,k,l} \xi_i^* \lambda_j^* \lambda_k \lambda_l m_j^\dagger m_k m_l e^{i(\delta_i + \delta_j - \delta_k - \delta_l)t} + \text{H.c.}$	$\chi^{(2)}$ nonlinearity
$\frac{\alpha}{2} \sum_{i,j,k,l} \lambda_i^* \lambda_j^* \lambda_k \lambda_l m_i^\dagger m_j^\dagger m_k m_l e^{i(\delta_i + \delta_j - \delta_k - \delta_l)t} + \text{H.c.}$	$\chi^{(3)}$ nonlinearity

The leading order contribution to  $\beta^{(1,2)}$  is zeroth order in both  $\lambda$  and  $\xi$ . The only terms in the Hamiltonian (S4) which contribute to  $\beta^{(1)}$  and  $\beta^{(2)}$  at this order are, respectively,

$$\left[ -\alpha (q^{\dagger 2} \xi_2 \lambda_A m_A + q^{\dagger 2} \xi_1 \lambda_B m_B) e^{-i(\delta_B + \delta_1)t} + \text{H.c.} \right] \quad \text{and} \quad \left[ -\alpha (q^{\dagger 2} \lambda_A m_A \lambda_C m_C + q^{\dagger 2} \xi_1 \lambda_B m_B) e^{-i(\delta_B + \delta_1)t} + \text{H.c.} \right] \quad (\text{S7})$$



The corrections from these terms can be calculated via standard perturbation theory,

$$\beta^{(1,2)} = \frac{\alpha}{\delta_B + \delta_1 + \alpha}.$$

For the **SWAP** operation, where the drives are far-detuned, this correction is typically negligible. However, for the **CZ** operation, this correction can significantly reduce the coupling rate since  $\delta_1, \delta_B$  can be comparable to  $\alpha$ . We note that the expression for  $\beta^{(1)}$  matches the leading order expression derived in Ref. [54].

Contributions to  $\beta^{(1,2)}$  at higher orders in  $\lambda$  can be neglected since we have assumed the dispersive regime,  $\lambda \ll 1$ . Contributions at higher orders in  $\xi$  can be systematically calculated with perturbation theory in principle, but such calculations quickly become tedious. Here, we employ an alternative approach. We consider the AC Stark shift type terms,  $-2\alpha \sum_j |\xi_j|^2 Q^\dagger Q$ , and compute their contributions to  $\beta^{(1,2)}$  nonperturbatively by working in a rotating frame.

Let  $S$  denote the qubit's AC Stark shift. In the frame where the qubit mode rotates at its Stark-shifted frequency,  $\tilde{\omega}_q = \omega_q + S$ , the system Hamiltonian is

$$H = -Sq^\dagger q + \sum_j \left[ \Omega_j q^\dagger e^{-i\tilde{\delta}_j t} + \text{H.c.} \right] + \sum_k \left[ g_k m_k q^\dagger e^{-i\tilde{\delta}_k t} + \text{H.c.} \right] - \frac{\alpha}{2} q^\dagger q q \quad (\text{S8})$$

where  $\tilde{\delta} = \omega - \tilde{\omega}_q$ . Performing unitary transformations analogous to those above eliminates the coupling and drive terms so that  $H = -S\tilde{Q}^\dagger \tilde{Q} - \frac{\alpha}{2} \tilde{Q}^\dagger \tilde{Q}^\dagger \tilde{Q} \tilde{Q}$ , where  $\tilde{Q} = q + \sum_j \tilde{\xi}_j e^{-i\tilde{\delta}_j t} + \sum_k \tilde{\lambda}_k m_k e^{-i\tilde{\delta}_k t}$ . Here,  $\tilde{\xi}_j = \Omega_j / \tilde{\delta}_j$  and  $\tilde{\lambda}_k = g_k / \tilde{\delta}_k$ . The Stark shift terms can then be cancelled by setting  $S = -2\alpha \sum_j |\tilde{\xi}_j|^2$  [74]. In the frame where the Stark shift terms are eliminated, one finds modified expressions for the corrections,

$$\beta^{(1)} = 1 - \frac{\delta_1 \delta_2 \delta_A \delta_B}{\tilde{\delta}_1 \tilde{\delta}_2 \tilde{\delta}_A \tilde{\delta}_B} \frac{\tilde{\delta}_B + \tilde{\delta}_1}{\tilde{\delta}_B + \tilde{\delta}_1 + \alpha} \quad (\text{S9})$$

$$\beta^{(2)} = 1 - \frac{\delta_1 \delta_A \delta_B \delta_C}{\tilde{\delta}_1 \tilde{\delta}_A \tilde{\delta}_B \tilde{\delta}_C} \frac{\tilde{\delta}_B + \tilde{\delta}_1}{\tilde{\delta}_B + \tilde{\delta}_1 + \alpha}. \quad (\text{S10})$$

Hence, the coupling rates are

$$g_v^{(1)} = -2\alpha \tilde{\xi}_1^* \tilde{\xi}_2 \tilde{\lambda}_A \tilde{\lambda}_B^* \frac{\tilde{\delta}_B + \tilde{\delta}_1}{\tilde{\delta}_B + \tilde{\delta}_1 + \alpha} \quad (\text{S11})$$

$$g_v^{(2)} = -2\alpha \tilde{\xi}_1^* \tilde{\lambda}_A \tilde{\lambda}_B^* \tilde{\lambda}_C \frac{\tilde{\delta}_B + \tilde{\delta}_1}{\tilde{\delta}_B + \tilde{\delta}_1 + \alpha}. \quad (\text{S12})$$

These expressions have the same form as above, but with the replacements  $\delta \rightarrow \tilde{\delta}$ , i.e. detunings are now defined relative to the qubit's Stark-shifted frequency. It follows that there also exists a Stark shift correction  $\beta^{(\gamma)}$  to the inverse-Purcell enhancement

$$\kappa_\gamma = \kappa + \gamma(g/\delta)^2(1 + \beta^{(\gamma)}), \quad (\text{S13})$$

where  $\beta^{(\gamma)} = (\delta/\tilde{\delta})^2 - 1$ , i.e.  $\kappa_\gamma = \kappa + \gamma(g/\tilde{\delta})^2$ . These corrections are important whenever the drives are strong enough that the qubit's Stark shift becomes comparable to the drive or mode detunings. Expressions (S11), (S12), and (S13) are used to produce the plots in this work.

### C. Comparison with numerical Floquet calculation

To assess the accuracy of the expressions (S11) and (S12), we compare with numerical calculations of the coupling rates using the methods developed in Ref. [54]. First, we briefly summarize the main results of that work. The authors consider the process of engineering a bilinear interaction between two microwave cavity modes that are mutually coupled to a transmon qubit. Treating the couplings as a perturbation, they calculate the linear response of the driven transmon. This perturbative treatment is justified in the dispersive regime. They show that  $g_v^{(1)}$  can be calculated in terms of a susceptibility matrix  $\chi^{(1)}(\omega_A, \omega_B; \omega_1, \omega_2)$ , that describes the response of the driven transmon at frequency  $\omega_A$  to a weak probe field at  $\omega_B$ , when subject to drives at  $\omega_1$  and  $\omega_2$ . The susceptibility can then be computed numerically to all orders in the drive amplitudes using Floquet theory. The authors find good quantitative agreement between their theoretical predictions and experimental results, even for strong drives ( $\xi > 1$ ).

This approach can be directly applied to calculate  $g_v^{(1)}$ . To calculate  $g_v^{(2)}$ , we analogously define a higher-order susceptibility matrix  $\chi^{(2)}(\omega_A, \omega_B, \omega_C; \omega_1)$  that captures the response of the transmon at frequency  $\omega_A$  to weak probes at  $\omega_B$  and  $\omega_C$ , when subject to a drive at  $\omega_1$ . Rather than computing  $\chi^{(2)}$  directly, which can be numerically tedious, we note that  $\chi^{(2)}$  can be computed in terms of  $\chi^{(1)}$ . In the calculation of  $\chi^{(1,2)}$ , the drives and probes are treated identically at the Hamiltonian level; both the drive and probe terms are of the form  $H = f_j q^\dagger e^{-i\omega_j t} + \text{H.c.}$ . For the drives,  $f_j = \Omega_j$ , while for the probes,  $f_j = gm_j$ . Since the susceptibility is calculated to all orders in the drive fields but only to leading order in the weak probe fields, going beyond leading order does not change the result in the limit where the field  $f_j$  is weak. Weak probes and weak drives are thus interchangeable, the only difference being a matter of interpretation. It follows that

$$\chi^{(2)}(\omega_A, \omega_B, \omega_C; \omega_1) = \chi^{(1)}(\omega_A, \omega_B; \omega_1, \omega_C). \quad (\text{S14})$$

This equivalence holds for  $g_C \ll \delta_C$ , which is the same limit that was already assumed to justify the perturbative treatment. Thus, the numerical procedure for calculation of  $g_v^{(1)}$  can also be straightforwardly applied to calculate  $g_v^{(2)}$ .

In Figs. S1(a) and (b), we calculate  $g_v^{(1,2)}$  numerically as described above, and we compare the results with the analytical expressions (S11) and (S12). Good agreement is observed for weak drives ( $\xi \lesssim 0.4$  for the parameters used in the plots). Discrepancies emerge at stronger drives, but this is expected because the corrections are obtained perturbatively. In Fig. S1 (c), (d), the coupling rates are plotted as a function of  $\delta_A$  to make apparent the importance of the AC Stark shift corrections. Due to the Stark shift, the corrected expressions and numerics are both red-shifted relative to the uncorrected expressions. Were the corrections not included, this relative shift would result in a systematic overestimation of the coupling rates for blue-detuned phonon modes.

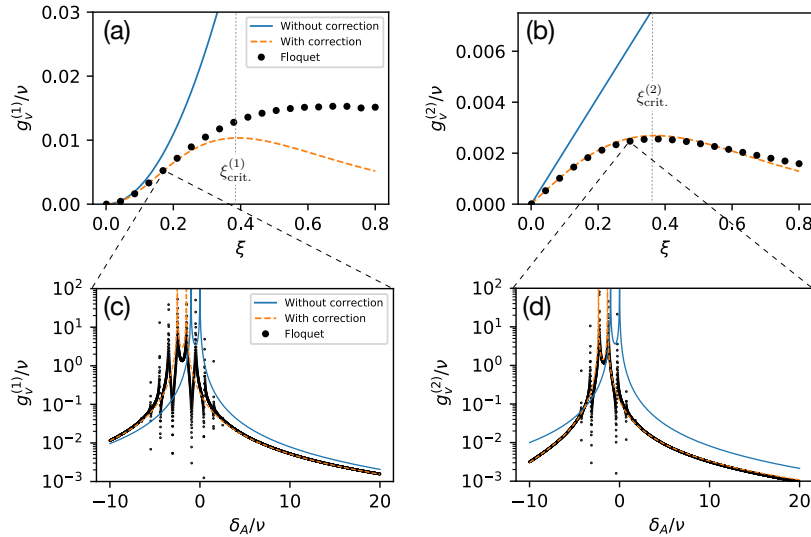


FIG. S1. Comparison of the coupling rate expressions with numerical Floquet calculations. (a), (b) Coupling rates  $g_v^{(1,2)}$  plotted as a function of drive strength. (c), (d) Coupling rates plotted as a function of the phonon mode detuning  $\delta_A$ . The uncorrected coupling rates exhibit two resonant peaks, at  $\delta_A = 0$  and  $\delta_A + \nu = \delta_B = 0$ , corresponding to resonant processes where phononic excitations in modes  $A$  or  $B$  are converted to transmon excitations. Because of the AC Stark shift, these peaks are red-shifted in both the numerical Floquet calculation and the corrected expressions. The additional resonant peaks in the numerical calculation correspond to multiphoton resonances where phononic excitations are converted to transmon excitations by exchanging an integer number of photons between the two drive fields [54]. It is important to carefully avoid these peaks in the experiments. Parameters for all plots match those in Fig. 3 of the main text:  $g_k/2\pi = 10\text{MHz}$ ,  $\delta_A/2\pi = 100\text{MHz}$ ,  $\nu/2\pi = 10\text{MHz}$ ,  $\Delta\nu = \nu/10$ . In order to account for the AC Stark shift, we also specify  $\alpha/2\pi = 150\text{MHz}$ , and we take  $\delta_1/2\pi = 1\text{GHz}$  in the calculation of  $g_v^{(1)}$ . In (c),  $\xi_{1,2} = 0.17$ , and in (d)  $\xi_1 = 0.27$ .

The AC Stark shift is responsible for the interesting non-monotonic behavior of expressions (S11) and (S12) with  $\xi$ . Intuitively, this behavior is explained by the fact that the Stark shift causes the qubit to move *away* from the phonon modes in frequency space. This reduces the participation of the phonons in the qubit mode, thereby reducing the coupling rate. When optimizing  $g_v$  so as to minimize the SWAP or CZ infidelity, the non-monotonicity effectively restricts the drive amplitudes to the range  $\xi \leq \xi_{\text{crit.}}$ , where  $\xi_{\text{crit.}}$  is the value of  $\xi$  for which  $g_v$  is maximal. For example, in Fig. 3 of the main text, the virtual couplings rates are restricted to  $|g_v^{(1)}|/2\pi < 100\text{kHz}$  and  $|g_v^{(2)}|/2\pi < 25\text{kHz}$ , in

accordance with the maximal values of  $g_v^{(1,2)}$  obtained in Fig. S1. Good agreement between the analytics and numerics is observed for  $\xi \lesssim \xi_{\text{crit.}}$ , validating the use of expressions (S11) and (S12).

The numerical calculations in Fig. S1 (a) suggest that  $g_v^{(1)}$  could be further increased by allowing  $\xi > \xi_{\text{crit.}}$ . To be conservative, however, we choose not to exploit this possibility; strong drives can induce deleterious processes such as the multiphoton resonances described in Ref. [54].

This comparison illustrates the importance of the corrections derived above and confirms that the virtual coupling rates are well-described by expressions (S11) and (S12) for the drive strengths considered in this work.

## II. ENGINEERING NONUNIFORM MODE SPACING

As discussed in the main text, nonuniform mode spacing is necessary in order to ensure that the resonance conditions are nondegenerate, i.e. to ensure that a given pair or triple of modes can be selectively coupled. In this section, we first formalize the meaning of nonuniform, then present several schemes for engineering nonuniformity in BAW and SAW systems—those in which modes are otherwise approximately uniformly spaced. For concreteness, we also provide example schematics for BAW and SAW devices with engineered nonuniformity. Note that phononic crystal resonators are not generally plagued by such degeneracies, since mode frequencies can be controlled by engineering the geometry of each individual phononic resonator.

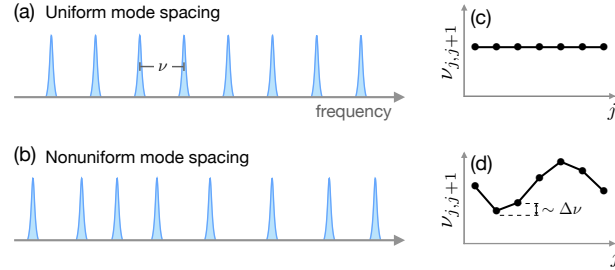


FIG. S2. Sets of (a) uniformly and (b) nonuniformly spaced modes. (c,d) The frequency differences between successive modes are plotted to illustrate the behavior of  $\nu_{j,j+1}$ . (c) For uniformly spaced modes,  $\nu_{j,j+1}$  is constant. (d) For nonuniformly spaced modes,  $\nu_{j,j+1}$  varies on the scale of  $\Delta\nu$ .

As shown in Fig. S2, a set of modes is nonuniformly spaced if there exist mode pairs  $\{i, j\}$  and  $\{k, \ell\}$  for which  $\nu_{ij} \neq \nu_{k\ell}$ , where  $\nu_{ij} = |\omega_i - \omega_j|$  is the frequency spacing between modes  $i$  and  $j$ . In the context of multimode coupling, it is useful to quantify this nonuniformity as follows. Let  $\mathcal{S}$  denote the set of all modes that are used to store quantum information, and let  $\mathcal{P}$  denote the set of all mode pairs that one chooses to couple (we provide examples below). The connectivity of the system is then described by a graph with vertices  $\mathcal{S}$  and edges  $\mathcal{P}$ . As a practically relevant measure of the nonuniformity, we define the quantity

$$\Delta\nu = \min_{\{i,j\} \in \mathcal{P}} \left[ \min_{\{k \in \mathcal{S}, \ell\} \neq \{i,j\}} |\nu_{ij} - \nu_{k\ell}| \right], \quad (\text{S15})$$

which lowerbounds the frequency selectivity of two-mode couplings. Explicitly, the beamsplitter resonance condition,  $\omega_2 - \omega_1 = \omega_B - \omega_A$  for a pair of modes  $\{A, B\} \in \mathcal{P}$  is detuned from all other beamsplitter resonance conditions involving any mode in  $\mathcal{S}$  by at least  $\Delta\nu$ . Highly selective virtual couplings thus require  $g_v/\Delta\nu \ll 1$ . Note that since  $\Delta\nu$  depends on the choices of  $\mathcal{S}$  and  $\mathcal{P}$ , there can exist a tradeoff between selectivity and the effective size and connectivity of the system. The definition of  $\Delta\nu$  can be straightforwardly generalized to the case of three-mode couplings.

Whether a given pair or triplet of modes can be selectively coupled depends on the structure of the nonuniformity, and in this regard it is convenient to classify different sorts of nonuniformity according to properties of  $\nu_{j,j+1}$ . We study two such classes in the examples below: *point defect nonuniformities*, for which  $\nu_{j,j+1}$  is constant except in the vicinity of a single defect, and *periodic nonuniformities*, for which  $\nu_{j,j+1}$  is periodic. Of course, other classes exist, but we focus on these two classes since instances can readily be engineered in cQAD systems.

### A. External mode hybridization

A point defect nonuniformity can be created by coupling the phonons to some external mode, such as a microwave resonator. As demonstrated in Ref. [45], and sketched in Fig. S3(a,b), the resulting mode hybridization can significantly shift phonon mode frequencies within some bandwidth  $\mathcal{D}$  of the external mode. The nonuniformity  $\Delta\nu$  is dictated by the magnitude of these frequency shifts. For example, frequency shifts of order 1MHz were demonstrated in Ref. [45].

This class of nonuniformity can enable selective coupling: selective two-mode coupling is possible if one or both involved modes lie in  $\mathcal{D}$ , and selective three-mode coupling is possible if two of the three involved modes lie in  $\mathcal{D}$ . Hence, the set  $\mathcal{S}$  can include arbitrarily many modes, but the set  $\mathcal{P}$  can only include mode pairs with at least one mode in  $\mathcal{D}$ . While modes outside of  $\mathcal{D}$  cannot be directly coupled to one another, information from these modes can instead be swapped into modes in  $\mathcal{D}$ , manipulated, and swapped back. Note that the coherence of the external mode should be comparable to that of the phonons, lest the hybridization result in a significant increase in effective decay rates, and in general there may exist a tradeoff between increased nonuniformity and enhanced decay.

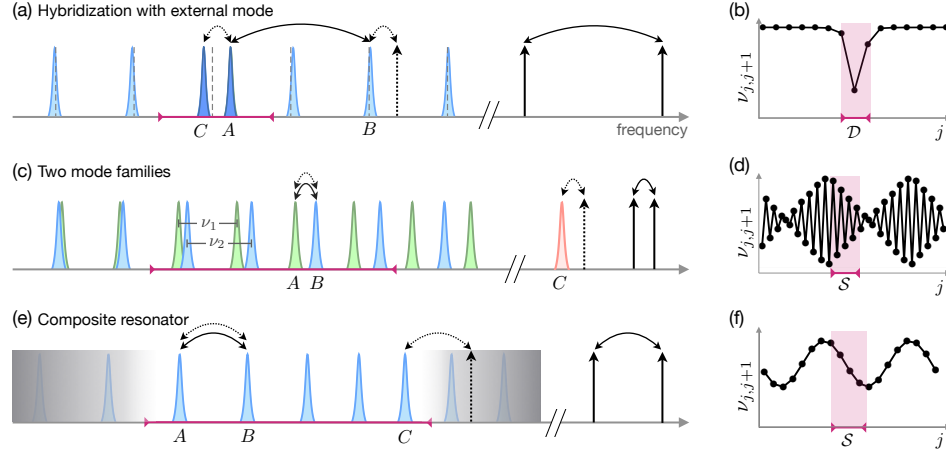


FIG. S3. Nonuniform mode spacing. (a) External mode hybridization. The coupling between phonons and an external mode causes strongly hybridized modes (dark blue) to deviate from the otherwise uniform spacing (dashed lines). The arrows show examples of how this nonuniformity gives rise to nondegenerate resonance conditions: modes  $A$  and  $B$  can be coupled by the applying drives indicated by solid arrows, while modes  $A$ ,  $B$ , and  $C$  can be coupled by applying the drive indicated by the dashed arrow. (b) Frequency differences shrink significantly within a bandwidth  $\mathcal{D}$  of the external mode. (c) Two mode families. Simultaneously coupling the transmon to two mode families (blue, green) enables selective two-mode coupling between modes from different families. Selectivity is only guaranteed in a finite region  $\mathcal{S}$ , and an example of such a region is highlighted in (d). The use of an external mode  $C$  enables selective three-mode coupling. (e) Composite resonator. Nonuniform mode spacing in composite resonators arises due to partial reflections at the interface(s). For example, with a single interface, a simple transfer matrix treatment [58] reveals that the FSR is periodically modulated, as in (f). Selective three-mode coupling can be enabled by restricting the transmon phonon-coupling bandwidth (regions with negligible coupling are shaded in gray), or by using an external mode as in (c).

### B. Two phonon mode families

Another approach is to create a periodic nonuniformity by simultaneously coupling the transmon to two families of phonon modes [18] with different free spectral ranges (FSRs). While modes within each family are uniformly spaced, the FSR difference causes the spacing between modes from different families to vary, as shown in Fig. S3(c,d). This nonuniformity enables two modes from different families to be selectively coupled, but because of the periodicity, selectivity is only guaranteed over a finite bandwidth smaller than one period. With two mode families, a set  $\mathcal{S}$  containing  $\approx \nu/\Delta\nu$  modes can be found wherein any two modes from different families can be selectively coupled with  $\Delta\nu = |\nu_1 - \nu_2|$ , where  $\nu_{1,2}$  are the FSRs of the two families.

By itself, the use of two mode families does not enable selective three-mode coupling [75], but this limitation can be circumvented by coupling the transmon to one or more external modes. For example, the BAW devices of Refs [16, 17] are housed in microwave cavities, and coupling the transmon to a high-Q cavity mode can enable selective three-mode coupling between the cavity and any pair of modes in  $\mathcal{S}$ . In a SAW device, the additional mode could come from another SAW resonator or a microwave resonator. The transmon itself could even serve as the external mode, but



gate fidelities would then be directly limited by transmon coherence. Ideally, the coherence of the external mode should be comparable to that of the phonons, lest it limit gate fidelity.

### C. Composite resonators

Yet another approach is to employ a composite acoustic resonator, in which phonons propagate in media with different indices of refraction [Fig. S3(e,f)]. Reflections at the interfaces can give rise to a periodic modulation of the FSR [58]. As in the case of two mode families, this periodic nonuniformity can enable selective two-mode coupling within a finite bandwidth  $\mathcal{S}$ , though the magnitudes of both  $\mathcal{S}$  and  $\Delta\nu$  depend on the nature of the modulation.

Whether selective three-mode coupling within  $\mathcal{S}$  is feasible depends on the of the specific nature of the FSR modulation. In cases where it is not already possible, selective three-mode coupling can be enabled by either coupling the transmon to some external mode, as previously described, or alternatively by restricting the bandwidth over which the transmon-phonon coupling is appreciable. For example, if the transmon-phonon coupling is only appreciable within  $\mathcal{S}$ , as in Fig. S3(e), then selective three-mode coupling is possible since the system contains an effectively finite number of nonuniformly spaced modes. In SAW systems, the coupling bandwidth can be tuned by changing the number of fingers in the interdigitated transducer [19, 42, 76]. In BAW systems, the coupling bandwidth can be similarly tuned by changing the electromechanical transducer's geometry. For instance, in a transducer comprised of alternating layers of piezoelectric and non-piezoelectric materials, the spacing, thickness, and number of such layers could be chosen so that the coupling has a narrow response centered at a particular frequency, as in a Bragg reflector.

### D. Example schematics

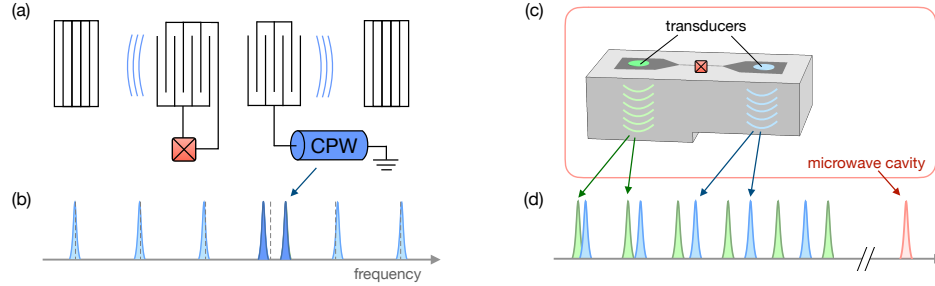


FIG. S4. SAW and BAW devices with engineered nonuniformity. (a) The modes of a SAW resonator are coupled to both a transmon and a coplanar waveguide (CPW) resonator. Hybridization with the resonator mode creates nonuniformity. (b) Mode frequencies of the device in (a). The CPW resonator mode and the phonon mode with which it most strongly hybridizes are shown in dark blue. (c) A 3D transmon couples to both a microwave cavity mode and to phonon modes from two BAW resonators with different FSRs (the difference is engineered by reducing the thickness of the substrate under one of the transducers). (d) Mode frequencies of the device in (c).

For concreteness, in Fig. S4 we provide example schematics for SAW and BAW devices in which nonuniformity is engineered according to the strategies described above. Fig. S4(a) shows a SAW device that exploits the external mode hybridization strategy. A SAW resonator is fabricated on a piezoelectric substrate, and coupling between the transmon and the phononic modes is enabled by an interdigitated capacitor. A superconducting coplanar waveguide resonator is also coupled to the phononic modes, and the hybridization of the phononic modes with the resonator mode creates the necessary nonuniformity.

Fig. S4(c) shows a BAW device that exploits the two mode families strategy. The device is based on those demonstrated in Refs. [16, 17]; a three-dimensional (3D) transmon is housed inside a microwave cavity, and thin disks of piezoelectric material (transducers) fabricated in the transmon's pads enable the transmon to couple to BAW modes in the substrate. Two modifications have been made relative to the devices in Refs. [16, 17]. First, an additional transducer has been added so that the transmon simultaneously couples to two families of modes. Second, the thickness of the substrate beneath one of the transducers has been reduced so that the two families have different FSRs. The microwave cavity mode, which dispersively couples to the transmon, provides the external mode necessary to enable selective three-mode couplings. We note that other elements, e.g. a separate readout resonator for the transmon, can be integrated into 3D architectures in such a way that the transmon can be driven and measured without involving the cavity mode [77].

### III. DETAILED DESCRIPTION OF THE CQAD QRAM

In this section we provide a more complete description of the qRAM proposed in the main text. The operation of the quantum quantum routers is first discussed in detail, and then schemes for extracting data from either a classical or a quantum database are presented.

#### A. Operation of a quantum router

During a qRAM query, the operation of each quantum router can be divided into four stages: initialization, downstream routing, upstream routing, and extraction. In the initialization stage [Fig. S5(a)], an incoming address qubit in the top mode is stored in the routing mode at the vertex so that it can control the routing of subsequent qubits. Initialization is performed simply by swapping the states of the top and routing modes. In the downstream routing stage [Fig. S5(b)], the router directs incoming qubits to one of two output modes conditioned on the state of the address qubit. As shown in the corresponding circuit, this routing operation can be implemented using a SWAP gate and a controlled-SWAP gate. Note that the action of the controlled-SWAP gate is trivial when the routing qubit is in  $|0\rangle$ . Similarly, the action of the SWAP gate is trivial when the routing qubit is in  $|1\rangle$ , since the affected modes are both in  $|0\rangle$  after the controlled-SWAP has been performed.

Once all downstream routing is complete and the data has been transferred to the bus, the inverse operations (upstream routing and extraction) must be performed in order to disentangle the address and bus qubits from the routers. Both the SWAP and controlled-SWAP unitaries are their own inverses, so the upstream routing [Fig. S5(c)] and extraction [Fig. S5(d)] operations can be implemented by time-reversing the downstream routing and initialization operations, respectively.

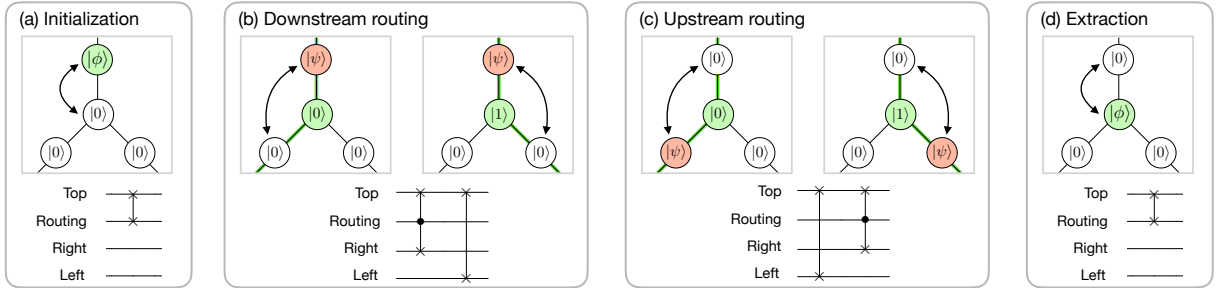


FIG. S5. Quantum router operation. (a) Initialization. An incoming address qubit  $|\phi\rangle$  is swapped into the routing mode. (b) Downstream routing. An incoming qubit  $|\psi\rangle$  is routed to the left(right) when the address qubit is in  $|0\rangle(|1\rangle)$ . (c) Upstream routing. The router directs a qubit from either the right or left mode into the top mode conditioned on the state of the address qubit. (d) Extraction. The address qubit is swapped into the top mode so that it can be routed back out of the tree.

#### B. Database access schemes

In a qRAM, the address and bus registers must necessarily be composed of qubits. However, the database itself can contain either classical or quantum data, depending on the intended application. How the database is accessed depends on the type of data. In the classical case, data can be directly copied into the bus, but in the quantum case the no-cloning theorem prevents one from copying quantum data. Instead, the bus can be entangled or swapped with the data, which generally leaves the address-bus system entangled with the database after a query. Additionally, while a qRAM should in general be able to both read from and write to the database, in many applications a quantum read-only memory (qROM) is sufficient [78–80]. This reduced functionality can be used to simplify the database access scheme. Below we present schemes for reading and writing both quantum and classical data, as well as a simplified scheme for read-only classical data.

Figure S6 illustrates procedures for accessing classical and quantum databases. To read quantum data from the database [Fig. S6(a)], we introduce a so-called pointer qubit, initially prepared in the state  $|1\rangle$ . The purpose of this qubit is to indicate which database entries should be extracted. After all address qubits have been routed into place, the pointer qubit follows their path to the bottom of the tree. Modes at the bottom of the tree then serve as controls

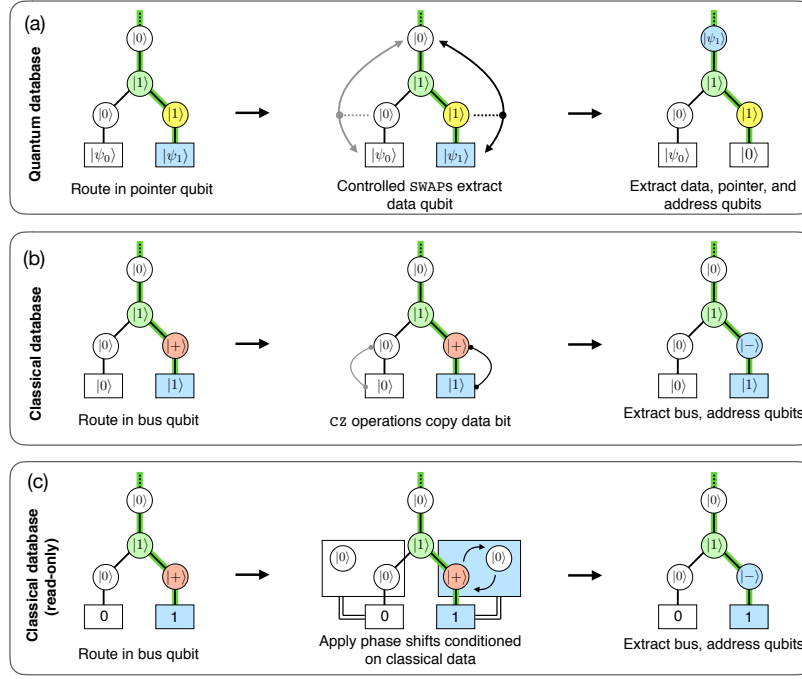


FIG. S6. Database access schemes for (a) quantum, (b) classical, and (c) classical read-only databases. (a) Quantum database access. A pointer qubit (yellow) is prepared in  $|1\rangle$  and routed to the bottom of the tree, following the path carved by the address qubits (green). Quantum data is stored in phononic modes, and the data is extracted via controlled-SWAP operations. The data, pointer, and address qubits are then sequentially routed out of the tree. (b) Classical database access. The bus qubit (red) is prepared in  $|+\rangle$  and routed to the bottom of the tree. Classical data is encoded in the  $|0, 1\rangle$  Fock states of phononic modes, and the data is copied to the bus via CZ operations. The bus and address qubits are then sequentially routed out of the tree. (c) Classical read-only database access. Classical data is stored in a purely classical memory array and copied to the bus by applying corresponding phase shifts to each mode at the bottom of the tree.

in controlled-SWAP operations that extract the desired data qubit. In each branch of the superposition, only the database entry adjacent to the pointer qubit is swapped out. The data, pointer, and address qubits are then routed out of the tree in sequence to complete the query. To write quantum data to the database [81], the entire procedure can be run in reverse. Note that, if a query is error-free, the pointer qubit remains in the state  $|1\rangle$  throughout and is disentangled from the rest of the system at the end of the query. Measuring this qubit after the query could thus provide a useful means of detecting errors.

In the classical case, a data bit  $D_j$  can be encoded in a mode as the Fock state  $|D_j\rangle$ . The operations described above for the quantum case then suffice to read or write classical data. However, since the read operation involves swapping out the data qubit, data is removed from the database during each query. In the classical case, data can instead be *copied* to the bus [Fig. S6(b)], which ensures that queries leave the database undisturbed. To copy data, the bus qubit is initially prepared in the state  $(|0\rangle + |1\rangle)/\sqrt{2} \equiv |+\rangle$ , and routed to the bottom of the tree. The desired classical bit is then copied to the bus by performing a CZ operation between the data and bus qubits; if  $|D_j\rangle = |0\rangle$ , the bus is unaffected, but if  $|D_j\rangle = |1\rangle$ , the CZ operation flips  $|+\rangle$  to  $|-\rangle$ , hence encoding the bit in the  $|\pm\rangle$  basis. Importantly, this operation does not disturb other modes, since these phase shifts leave the state  $|0\rangle$  unaffected. The bus and address qubits are then routed out of the tree to complete the query.

In the classical read-only case [Fig. S6(c)], it is not necessary to encode data in the Fock states of phonon modes. Instead, the entire database can be stored in a purely classical memory array so that it is not susceptible to decoherence. To query such a database, the bus is again prepared in  $|+\rangle$  and routed to the bottom of the tree. The desired classical bit is copied to the bus by applying phase shifts to each mode at the bottom of the tree in accordance with the database entries. If  $D_j = 1$ , a phase shift of  $-1$  is applied to the  $j^{\text{th}}$  mode, and if  $D_j = 0$ , no phase shift is applied. As discussed in the main text, phase shifts can be imparted to a mode by tuning the relative driving phases during a consecutive sequence of two SWAP operations with an ancillary mode.